ACS APPLIED ENERGY MATERIALS

www.acsaem.org Article

Structure–Property Relationships in High-Rate Anode Materials Based on Niobium Tungsten Oxide Shear Structures

Luke D. Salzer, Brian Diamond, Kelly Nieto, R. Colby Evans, Amy L. Prieto, and Justin B. Sambur*

Cite This: https://doi.org/10.1021/acsaem.2c03573 Read Online

ACCESS | Metrics & More | Article Recommendations | Supporting Information

ABSTRACT: $Nb_{16}W_5O_{55}$ emerged as a high-rate anode material for Li-ion batteries in 2018 [Griffith et al., *Nature***2018**, *559* (7715), 556–563]. This exciting discovery ignited research in Wadsley–Roth (W–R) compounds, but systematic experimental studies have not focused on how to tune material chemistry and structure to achieve desirable properties for energy storage applications. In this work, we systematically investigate how structure and composition influences capacity, Li-ion diffusivity, charge–discharge profiles, and capacity loss in a series of niobium tungsten oxide W–R compounds: (3 × 4)-$Nb_{12}WO_{33}$, (4 × 4)-$Nb_{14}W_3O_{44}$, and (4 × 5)-$Nb_{16}W_5O_{55}$. Potentiostatic intermittent titration (PITT) data confirmed that Li-ion diffusivity increases with block size, which can be attributed to an increasing number of tunnels for Li-ion diffusion. The small (3 × 4)-$Nb_{12}WO_{33}$ block size compound with preferential W ordering on tetrahedral sites exhibits single electron redox and, therefore, the smallest measured capacity despite having the largest theoretical capacity. This observation signals that introducing cation disorder (W occupancy at the octahedral sites in the block center) is a viable strategy to assess multi-electron redox behavior in (3 × 4) $Nb_{12}WO_{33}$. The asymmetric block size compounds [i.e., (3 × 4) and (4 × 5) blocks] exhibit the greatest capacity loss after the first cycle, possibly due to Li-ion trapping at a unique low energy pocket site along the shear plane. Finally, the slope of the charge–discharge profile increases with increasing block size, likely because the total number of energy-equivalent Li-ion binding sites also increases. This unfavorable characteristic prohibits the large block sizes from delivering constant power at a fixed C-rate more so than the smaller block sizes. Based on these findings, we discuss design principles for Li-ion insertion hosts made from W–R materials.

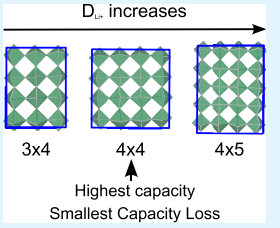

KEYWORDS: *energy storage, transition metal oxides, Li-ion diffusivity, structure–property relationships, high-rate energy, Wadsley–Roth phases*

INTRODUCTION

One limitation of graphite anodes in Li-ion batteries is Li metal grows from the electrode surface when the cell is cycled at high rates, resulting in catastrophic failure when metallic dendrites pierce the separator and contact the cathode.[2−5] Transition metal oxides are being explored as safe alternatives to graphite because lithium dendrite formation does not occur under fast charge/discharge conditions.[6,7] Of the potential candidates [e.g., TiO_2, Nb_2O_5, and $Li_4Ti_5O_{12}$ (LTO)], Wadsley–Roth (W–R) crystallographic shear structures are attractive anode materials because they exhibit multi-electron redox (beyond 1.0 Li^+/transition metal) and extraordinarily fast Li-ion diffusion coefficients (D_{Li+}) that are 2 orders of magnitude greater than commercialized LTO.[1,8] Griffith et al. showed that the power density of an un-optimized W–R compound, $Nb_{16}W_5O_{55}$, exceeded that of optimized graphite.[1] This discovery inspired substantial research efforts to understand how the unique structural features of niobium tungsten oxide (NbWO) W–R materials contribute to their high-rate capability in a Li-ion battery.

W–R shear structures consist of $n \times m$ blocks of corner-sharing octahedra connected to neighboring blocks via edge-sharing octahedra (see Scheme 1).[9−12] The blocks extend indefinitely in the direction perpendicular to the $n \times m$ block plane. In some structures, tetrahedral sites are present at the block corners to fill voids. These W–R phases exhibit many low-energy Li-ion binding sites within the large tunnels of the block structure (Scheme 1).[13,14] The large number of energy equivalent sites results in low, 0.2–0.3 eV, activation barriers for Li-ion diffusion and room temperature D_{Li+} values on the order of 1×10^{-12} to 1×10^{-11} m^2/s, highly competitive with state-of-the-art solid-state electrolytes.[13,15]

In principle, vast parameter space exists to optimize functional properties via their chemistry, stoichiometry, block size, and characteristic block joining,[12] but few systematic studies focusing on structure–property relationships exist for this exciting class of high-rate energy storage materials. For example, the literature hypothesis states that Li-ion diffusivity increases with increasing W–R block size due to the number of energy-equivalent tunnels for long-range lithium diffusion.[14] Evaluating this hypothesis is significant because it would

Received: November 2, 2022
Accepted: January 3, 2023
Published: January 13, 2023

Scheme 1. Crystal Structures of (a) (3 × 4)-$Nb_{12}WO_{33}$, (b) (4 × 4)-$Nb_{14}W_3O_{44}$, and (c) (4 × 5)-$Nb_{16}W_5O_{55}$[a]

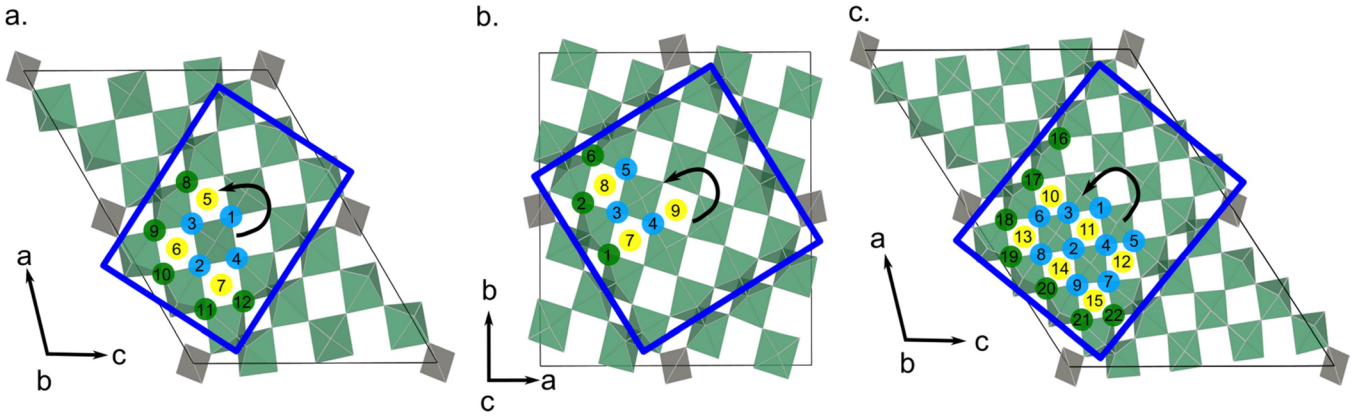

[a]The gray and green polyhedra represent the tetrahedral and octahedral coordination environments, respectively. The blue lines indicate the shear planes and define the block size. The green, yellow, and blue numbered circles represent the pocket, horizontal window, and vertical window Li-ion binding sites, respectively, according to Koçer et al.[14] [Arrows indicate twofold rotation in (a) (3 × 4)-$Nb_{12}WO_{33}$ and (c) (4 × 5)-$Nb_{16}W_5O_{55}$ and a fourfold rotation in (b) (4 × 4)-$Nb_{14}W_3O_{44}$.]

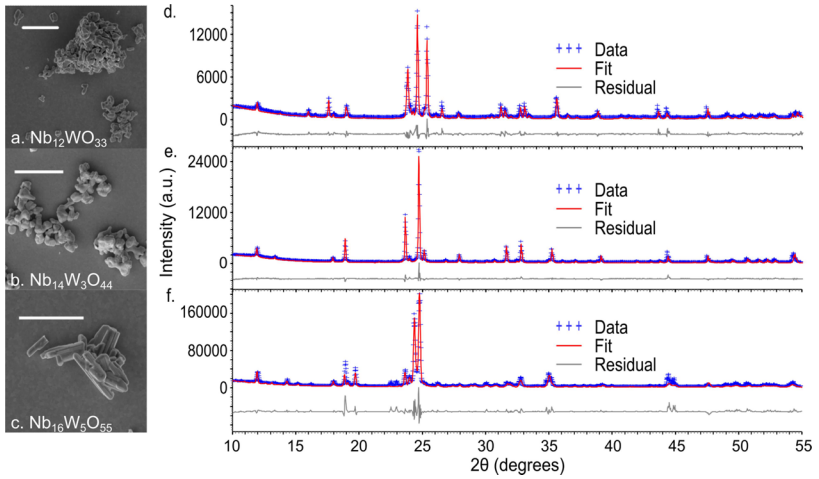

Figure 1. Morphology and structural characterization of niobium tungsten oxide W–R compounds. (a–c) SEM images and (e,f) XRD data of (3 × 4)-$Nb_{12}WO_{33}$, (4 × 4)-$Nb_{14}W_3O_{44}$, and (4 × 5)-$Nb_{16}W_5O_{55}$. The solid red lines represent Rietveld refinement results. All scale bars in (a–c) are 10 μm.

establish a key structure/property relationship for researchers developing fast-charging W–R materials. Furthermore, theoretical capacity decreases with increasing block size (Figure S1), but this trend has not been experimentally validated. Confirming this theoretical capacity trend could aid materials discovery efforts by pinpointing a block size from which to tune chemistry and stoichiometry.

Several research groups have investigated NbWO W–R compounds (e.g., $Nb_{12}WO_{33}$,[12,16,17] $Nb_{26}W_4O_{77}$,[18,19] $Nb_{14}W_3O_{44}$,[12,19,20] $Nb_{16}W_5O_{55}$,[1] and $Nb_{18}W_8O_{69}$[15]), but the performance metrics obtained from those studies reflect a mixture of bulk and nanoscale/structured materials in different electrode formulations and configurations. Capacity loss has been reported in $Nb_{12}WO_{33}$, $Nb_{14}W_3O_{44}$, and $Nb_{16}W_5O_{55}$,[1,20,21] but systematic studies have not focused on the possible Li-ion trapping sites in the different block compounds. In summary, no systematic studies exist that compare functional properties (e.g., capacity, charge/discharge profiles, ionic diffusivity, and capacity loss) versus block size for a nominally equivalent particle morphology and electrochemical cell design.

In this work, we systematically investigated the capacity, capacity loss, charge–discharge curves, and D_{Li+} as a function of block size in the Nb_2O_5-WO_3 system using (3 × 4)-$Nb_{12}WO_{33}$, (4 × 4)-$Nb_{14}W_3O_{44}$, and (4 × 5)-$Nb_{16}W_5O_{55}$. We focused on these compounds because they share the same block connectivity (i.e., joined by a tetragonal site at the block corners, Scheme 1). Keeping this structural motif consistent is important because the blocks connected by tetragonal sites have different Li-ion binding sites than those that do not.[12] We confirmed the literature hypothesis that D_{Li+} increases with block size. However, the charge/discharge profile becomes steeper and steeper with increasing block size, which hinders those compounds from delivering constant power. We discuss trends in capacity and capacity loss that can be attributed to structural features among the Nb_2O_5–WO_3 series.

RESULTS AND DISCUSSION

W–R compounds were synthesized via high-temperature solid-state reactions.[1,9,12] Different compositions were assessed by adjusting the mole ratio and heating rate (see Methods for details).[9,12,15] In a typical reaction, stoichiometric ratios of

https://doi.org/10.1021/acsaem.2c03573
ACS Appl. Energy Mater. XXXX, XXX, XXX–XXX

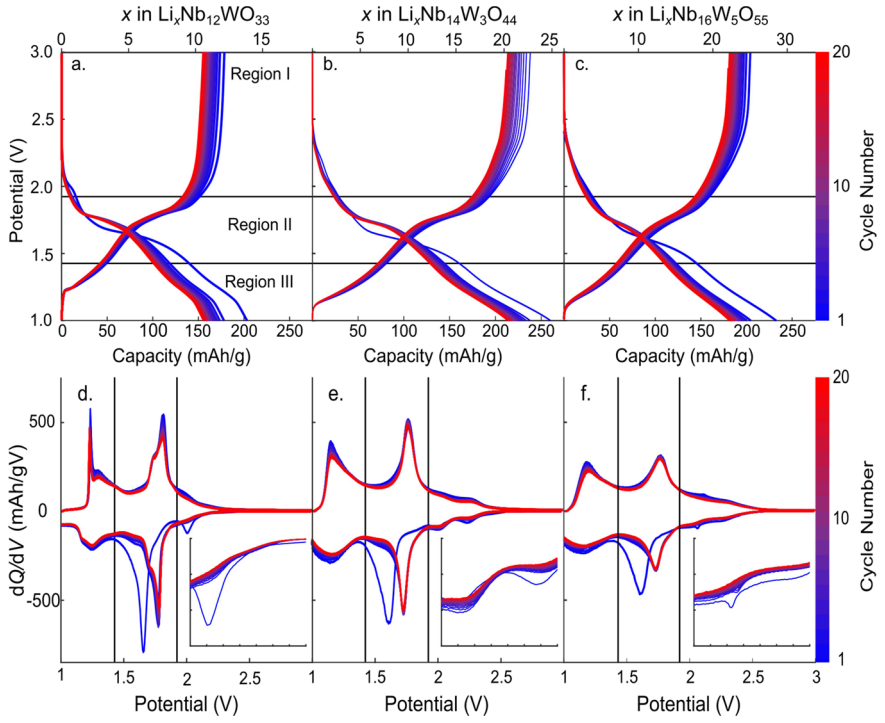

Figure 2. Charge/discharge curves (20 cycles at C/3) of (a) $Nb_{12}WO_{33}$, (b) $Nb_{14}W_3O_{44}$, and (c) $Nb_{16}W_5O_{55}$ and differential capacity plots of (d) $Nb_{12}WO_{33}$, (e) $Nb_{14}W_3O_{44}$, and (f) $Nb_{16}W_5O_{55}$. Insets in (d–f) represent the potential range from 1.95 to 2.30 V.

NbO_2 and $WO_{2.9}$ precursors were ground by hand using a mortar and pestle, pressed into a pellet, loaded into a platinum crucible, and heated to 1200 °C in air. The powder products were ground in a mortar and pestle for powder X-ray diffraction (XRD) and scanning electron microscopy (SEM) analyses. Figure 1 shows XRD data and SEM images of the reaction products that targeted (3 × 4)-$Nb_{12}WO_{33}$ (space group *C*2), (4 × 4)-$Nb_{14}W_3O_{44}$ (space group *I*4/*m*), and (4 × 5)-$Nb_{16}W_5O_{55}$ (space group *C*2). Rietveld refinement indicated each sample's phase purity exceeded 90%, consistent with Griffith et al.,[22] as well as the following trends that have important consequences for multi-electron redox behavior discussed below: (1) preference for W^{6+} at the tetrahedral site for $Nb_{12}WO_{33}$, (2) W^{6+} occupancy at the octahedral sites in the block center for (4 × 4)-$Nb_{14}W_3O_{44}$ and (4 × 5)-$Nb_{16}W_5O_{55}$, and (3) and significant cation disorder for (4 × 4)-$Nb_{14}W_3O_{44}$ and (4 × 5)-$Nb_{16}W_5O_{55}$.[14,15,23]

The reactions produced samples with nearly equivalent particle morphologies (Figure 1a–c), specifically micron-size particles with subhedral to euhedral columnar crystal shape, in agreement with the literature.[1,15] The major axis dimensions of (3 × 4)-$Nb_{12}WO_{33}$ and (4 × 4)-$Nb_{14}W_3O_{44}$ samples were nearly identical (1.1 ± 0.2 and 1.2 ± 0.3 μm, respectively, for N = 100 particles and the error represents the standard deviation). The average particle size of the (4 × 5)-$Nb_{16}W_5O_{55}$ sample was slightly larger (1.7 ± 0.4 μm, N = 100). In summary, we synthesized a series of WR samples with similar particle size and morphology so we could compare how the electrochemical properties and ionic diffusivity trends change with increasing block size.

Next, we evaluated the electrochemical properties of the W–R compounds as Li-ion insertion hosts under nearly identical conditions. We designed electrodes and chose experimental procedures that maximized the possibility of observing how electrochemical properties change with block size, rather than optimizing battery performance. To do so, we constructed coin cells using an 8:1:1 ratio of active material, conductive carbon, and binder because this ratio has been shown to minimize ohmic losses of the intrinsically poorly conducting oxide particles.[24,25] Additionally, we employed slow galvanostatic cycling conditions (<C/3) that further minimize ohmic losses and to reveal key features in differential capacity plots that are obscured at high C-rates.

Figure 2a–c shows the (dis)charge curves for (3 × 4)-$Nb_{12}WO_{33}$, (4 × 4)-$Nb_{14}W_3O_{44}$, and (4 × 5)-$Nb_{16}W_5O_{55}$, respectively. For all compounds, the discharge curve can be divided into three potential regions (denoted by horizontal lines in Figure 2a–c and vertical lines in Figure 2d–f). We discuss the (dis)charge curve of (3 × 4)-$Nb_{12}WO_{33}$ only because all compounds exhibit the following characteristics. In Region I (Figure 2a), the potential rapidly decreases from 3.0 to 2.0 V vs Li/Li^+ with increasing x in $Li_xNb_{12}WO_{33}$ until an inflection point occurs at x = 1. Then, in Region II, the potential gradually drops from 1.90 to 1.75 V with increasing lithiation content until x = 10. Finally, in Region III, the potential decreases to 1.0 V. The first discharge capacity is 203 mAh/g, in agreement with literature values for samples synthesized via a high temperature solid state reaction.[16] Upon de-lithiation of (3 × 4)-$Nb_{12}WO_{33}$, the potential quickly increases from 1.00 to 1.19 V. In Region II, the potential monotonically increases until an inflection point occurs at approximately 1.80 V. Lastly, the potential increases rapidly in Region III from 2.0 to 3.0 V vs Li/Li^+. The first charge capacity is 179 mAh/g, corresponding to 88% coulombic efficiency (CE) after the first cycle (Figure S2). The low CE after the first cycle suggests irreversible Li-ion trapping in the host, which has been suggested in the literature[13] and will be discussed below.

One noticeable trend in the charge–discharge profiles is the increasing sloping profile from left to right in Figure 2a–c,

https://doi.org/10.1021/acsaem.2c03573
ACS Appl. Energy Mater. XXXX, XXX, XXX–XXX

which manifests in peak broadening for the Region II peak in the dQ/dV plots (Figure 2d–f). We observe a strong positive correlation between the full width at half-maximum of the Region II peak and the total number of Li-ion binding sites in the unit cell (Figure S3). Hence, introducing a larger number of energy-equivalent Li-ion binding sites likely causes the redox reactions to occur over a broader range of potentials, inducing a steeper voltage profile with increasing block size. The observation indicates a structural limitation of the large block-size compounds because flat voltage profiles are highly desirable for delivering constant power in energy storage applications. One strategy to address this sloping voltage profile issue is to tune the redox potentials of the Li-ion binding sites via transition metal doping in the block center or along the shear plane.

Another critical observation from the cycling data in Figure 2 is that the measured capacity does not decrease with block size. We expected to observe a monotonic decrease in capacity with the increasing block size (Figure S1). However, (4 × 4)-$Nb_{14}W_3O_{44}$ exhibited the highest specific discharge capacity upon lithiation (260 mAh/g after first discharge), while (3 × 4)-$Nb_{12}WO_{33}$ and (4 × 5)-$Nb_{16}W_5O_{55}$ exhibited 203 and 232 mAh/g, respectively (Figure 2a–c). To understand the origin of our observations, we examined the ratio of measured capacity to theoretical capacity assuming 1 Li^+/transition metal (Figure S4), including literature data for (5 × 5)-$Nb_{18}W_8O_{69}$ synthesized via a high temperature solid state reaction.[15] Interestingly, (3 × 4)-$Nb_{12}WO_{33}$ is the only compound that does not exhibit multielectron redox; all other compounds exhibit approximately 1.4 Li^+/transition metal. The structurally unique feature of (3 × 4)-$Nb_{12}WO_{33}$ is W ordering on the tetrahedral sites, in agreement with the literature and observed in our Rietveld analyses.[14] As the block size increases, the probability of W occupancy in the block center increases.[14] Since X-ray absorption spectroscopy measurements of (4 × 5)-$Nb_{16}W_5O_{55}$ clearly show that W is responsible for multi-electron redox behavior, we conclude that (3 × 4)-$Nb_{12}WO_{33}$ exhibits lower capacity than the larger block compounds because tetrahedral W sites do not contribute to multi-electron redox behavior.[1] We attempted to provide direct evidence for the aforementioned hypothesis using ex-situ XPS analysis on $Nb_{12}WO_{33}$ following charge/discharge cycling. However, the F 2s, N 4p, and W 4f peaks overlap, making quantitative peak analysis challenging with our in-house XPS. Indirect evidence for this hypothesis exists in the literature. For example, Saritha et al. compared the capacity of (3 × 4)-$Nb_{12}WO_{33}$ electrodes synthesized via a high temperature solid state reaction and a low-temperature sol–gel route, which reached approximately 19 Li^+/transition metal.[16] The authors observed discharge capacities greater than 1 Li^+/transition metal for the sol–gel material, which we believe stems from cation disorder in the material synthesized at low temperature (W occupancy in the block center). Yan et al. also observed multi-electron redox (1.2 Li^+/transition metal) in nanostructured (3 × 4)-$Nb_{12}WO_{33}$ synthesized via electrospinning followed by sintering at 1000 °C, where significant cation disorder may also be present in the material.[17] In summary, we hypothesize that W occupancy in the block center is responsible for multi-electron redox behavior in the larger block sizes. Introducing W disorder in (3 × 4)-$Nb_{12}WO_{33}$ materials could be a viable strategy to assess >1 Li^+/transition metal.

Next, we analyzed the capacity loss trends as a function of block size (Figure 3). The asymmetric block compounds [e.g., $m \neq n$ in (3 × 4)-$Nb_{12}WO_{33}$ and (4 × 5)-$Nb_{16}W_5O_{55}$] exhibit greater capacity loss than the symmetric (4 × 4)-$Nb_{14}W_3O_{44}$ material. Specifically, (3 × 4)-$Nb_{12}WO_{33}$ and (4 × 5)-$Nb_{16}W_5O_{55}$) show >12% capacity loss, whereas (4 × 4)-$Nb_{14}W_3O_{44}$ exhibits 8% capacity loss. Figure S5 shows additional cycling data for multiple coin cells. Distinct features appear in the dQ/dV plots of the "asymmetric" block structure compounds [i.e., (3 × 4) and (4 × 5)] that could explain the structural origin of the greater capacity loss. The asymmetric block compounds exhibit a single, sharp irreversible peak in Region I of the initial discharge cycle of the dQ/dV plots (inset Figure 2d,f-insets). On the other hand, (4 × 4)-$Nb_{14}W_3O_{44}$ and (5 × 5)-$Nb_{18}W_8O_{69}$ exhibit two broad and relatively more reversible peaks in Region I (Figure 2e-inset and ref 15). We hypothesize that (3 × 4)-$Nb_{12}WO_{33}$ and (4 × 5)-$Nb_{16}W_5O_{55}$ exhibit one peak in Region I because 1 Li^+ inserts into a low energy fivefold coordinated "pocket" site at the shear plane (site 12 in Scheme 1a and site 17 in Scheme 1c). Koçer et al.'s first-principle calculations suggested that this pocket site is a low energy, highly stable Li-ion binding site that is likely responsible for ion trapping in NWO compounds.[13] An alternative possibility is that the first Li-ion inserts in the symmetry unique site in the block center of the asymmetric compounds (site 1 in Scheme 1a,c). Our results provide insight into how unit cell symmetry may affect capacity retention in W–R phases, but future systematic studies are needed to elucidate the lithiation mechanism and site ordering. Regardless of the exact origin of the capacity loss, we hypothesize that tuning the composition of "symmetric" WR compounds [e.g., (4 × 4)-$Nb_{14}W_3O_{44}$ and (5 × 5)-$Nb_{18}W_8O_{69}$] is a viable strategy to achieve desired properties (e.g., multi-electron redox) with minimal capacity fade.

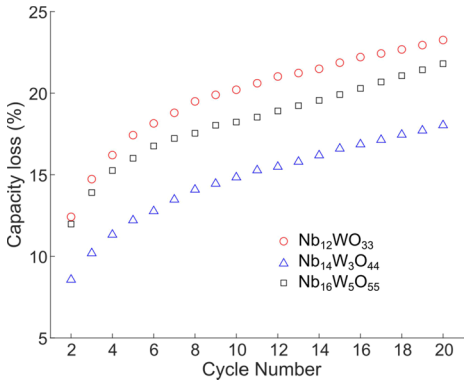

Figure 3. Capacity loss, defined as the discharge capacity for each cycle divided by the first discharge capacity, for (3 × 4)-$Nb_{12}WO_{33}$, (4 × 4)-$Nb_{14}W_3O_{44}$, and (4 × 5)-$Nb_{16}W_5O_{55}$.

Finally, we tested the literature hypothesis that Li-ion diffusivity increases with increasing block size.[15] To do so, we performed potentiostatic intermittent titration (PITT) measurements on cycled coin cells (see Methods) to minimize the influence of cycle-dependent performance that occurs for freshly made coin cells. Adapting the approach of Aurbach et al.,[26] we applied 25 mV potential steps from 1.0 to 2.0 V and fit the current–time data for t > 30 min. This condition yields a slope equal to $\frac{D_{Li^+}\pi^2}{4L^2}$,[27] where L is the particle length. In this work, we define L as half the major axis dimension as determined by particle size analysis (N = 100 particles) from SEM images. We focus on PITT measurements starting from the unlithiated state because the compounds are more

https://doi.org/10.1021/acsaem.2c03573
ACS Appl. Energy Mater. XXXX, XXX, XXX–XXX

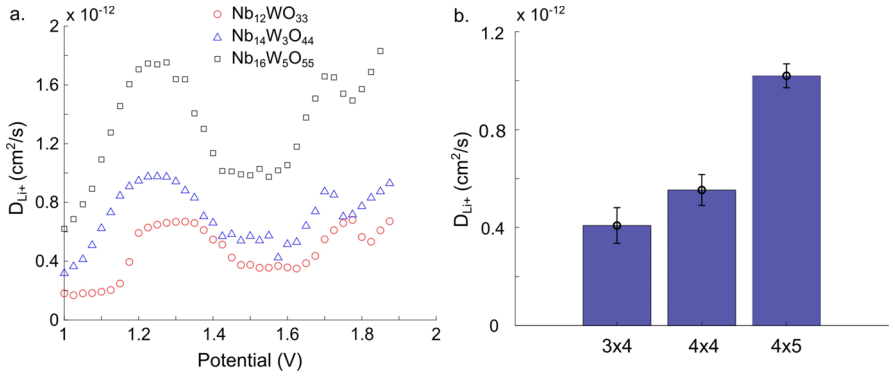

Figure 4. (a) Li-ion diffusion coefficient versus applied potential, as determined via PITT measurements for the cathodic sweep from 1.0 to 2.0 V. (b) Average D_{Li+} values for the potential range of 1.4−1.6 V (error bars indicate standard deviation).

electronically conducting in the lithiated condition, and we suspect the insulating nature of the intrinsic oxides could influence the D_{Li+} values when the potential is swept from 2.0 to 1.0 V. Figure 4a shows the resulting D_{Li+} values versus potential for (3 × 4)-$Nb_{12}WO_{33}$, (4 × 4)-$Nb_{14}W_3O_{44}$, and (4 × 5)-$Nb_{16}W_5O_{55}$. D_{Li+} values show a peak-like feature between 1.2 and 1.3 V, in agreement with the literature, and then remain approximately potential independent over the range of 1.5−2.0 V.[1,13,17] The D_{Li+} peak feature could be due to the unique lattice expansion mechanism with increasing x. The average Li-ion diffusion coefficient over the potential range of 1.4−1.6 V increases with increasing block size (Figure 4b), confirming the literature hypothesis that increasing the number of energy-equivalent tunnels in the block structure increases Li-ion diffusivity. This important structure−property relationship holds whether performing PITT experiments or analyses starting from the lithiated state (Figure S6).

CONCLUSIONS

We synthesized a series of NbWO W−R compounds to investigate how block size influences electrochemical properties and performance metrics of interest for high-rate electrochemical energy storage applications. The D_{Li+} values increase with increasing block size, suggesting that the larger block-size compounds may be superior anode materials for high-rate applications. However, increasing block size does not lead to a monotonic increase in capacity: (4 × 4)-$Nb_{14}W_3O_{44}$ possesses the largest discharge capacity, followed by (4 × 5)-$Nb_{16}W_5O_{55}$ and (3 × 4)-$Nb_{12}WO_{33}$. The low capacity for the (3 × 4)-$Nb_{12}WO_{33}$ compound stems from its inability to assess multi-electron redox behavior, further signaling that octahedral W sites are responsible for multi-electron redox behavior in the larger block sizes. Furthermore, the block symmetry affects capacity retention: the asymmetric (3 × 4)-$Nb_{12}WO_{33}$ and (4 × 5)-$Nb_{16}W_5O_{55}$ compounds exhibit greater capacity loss, likely due to a low energy Li-ion trapping site along the shear plane. Lastly, WR compounds with larger block sizes exhibit steeper and steeper charge/discharge profiles, which limits their ability to deliver constant power in energy storage applications. This sloping voltage profile trend may be due to the larger block sizes possessing more lithium storage sites with a broader range of Li-ion binding energies and environments. The structure−property relationships reported herein should extend to other W−R compounds and, therefore, guide the development of novel W−R compositions for electrochemical energy storage applications.

METHODS

Synthesis and Structure Characterization. The samples were produced using high temperature solid-state synthesis following literature protocols.[1,9,12] All three compositions were synthesized from stoichiometric ratios of NbO_2 (Alfa Aesar) and $WO_{2.9}$ (Alfa Aesar); for example, 1.64 g of NbO_2 and 0.25 g of $WO_{2.9}$ were required to synthesize (3 × 4)-$Nb_{12}WO_{33}$. The solid powders were ground in an agate mortar and pestle and pressed into a pellet using a hydraulic press (Caver Model: 4350.L) at 2 tons of pressure. The pellets were placed in a platinum crucible and heated in the air in a Thermo Scientific Lindberg Blue M tube furnace. To assess the (3 × 4)-$Nb_{12}WO_{33}$ and (4 × 4)-$Nb_{14}W_3O_{44}$ compounds, the pellets were heated from 25 to 1200 °C over a 10 h period (2 °C/min) and then cooled to 25 °C in 10 h. The (4 × 5)-$Nb_{16}W_5O_{55}$ compound was prepared by heating the pellet from 25 to 1200 °C at 10 °C/min and cooling to 25 °C. The pellets were ground using a mortar and pestle before materials characterization. The samples were characterized by powder XRD using a Bruker D8 Discover DaVinci − Powder Diffractometer (Cu Kα radiation). SEM analyses were performed on a JEOL 6500 field emission SEM.

Battery Assembly and Electrochemical Measurements. Half-cell batteries were constructed in an argon glove box using stainless steel coin cells (MTI, CR2032 cases, with a polypropylene sealing gasket), a stainless-steel conical spring, a stainless-steel spacer, a polypropylene (MTI Corp), and glass microfiber (Whatman) separator. These electrodes had an active material/carbon/binder mass ratio of 8:1:1. The metal oxide, conductive carbon (Super P), and polyvinylidene fluoride binder were hand ground in an agate mortar and pestle. The mixture was dispersed in N-methyl pyrrolidone (NMP, Sigma-Aldrich) before doctor-blading a 100 μm thick film on a copper substrate and dried in a vacuum oven overnight at 150 °C. The dried half cells were punched into 1/2 inch electrodes. These electrodes served as the cathode and lithium metal served as the anode. The electrolyte containing 1 M $LiPF_6$ dissolved in a 1:1 volume ratio of ethylene carbonate/dimethyl carbonate (EC/DMC, Sigma Aldrich) was dropped (approximately 80 μL) onto the separators. The cells were then pressed with 0.9 tons of pressure using a compact digital pressure-controlled electric crimper (MTI MSK-160E).

The coin cells were cycled on an Arbin battery tester (LBT-20084) using the following procedure. The cells rested for 12 h prior to cycling so that the added electrolyte had adequate time to saturate the separators. Following the resting period, the cells were cycled at low C-rates (<C/3), which was calculated for each compound using its theoretical capacity for one-electron transfer per transition metal. The potential window for galvanostatic cycling was 1.0 to 3.0 V vs Li^+/Li.

PITT measurements were conducted using a CHI potentiostat (Model 1200 series) over the potential range of 1.0 to 2.0 V vs Li/Li^+ in potential steps of 25 mV. The current for each potential step was measured for 45 min. We fit the i−t response for t > 30 min,

https://doi.org/10.1021/acsaem.2c03573
ACS Appl. Energy Mater. XXXX, XXX, XXX−XXX

according to the literature.[26,27] A 15 min wait time was applied after each potential step to allow the cell to reach steady state conditions.

■ ASSOCIATED CONTENT

Supporting Information

The Supporting Information is available free of charge at https://pubs.acs.org/doi/10.1021/acsaem.2c03573.

Additional capacity retention data, PITT measurements, and theoretical capacity plots (PDF)

■ AUTHOR INFORMATION

Corresponding Author

Justin B. Sambur − *Department of Chemistry, Colorado State University, Fort Collins, Colorado 80523, United States;* orcid.org/0000-0002-8457-4946; Email: jsambur@colostate.edu

Authors

Luke D. Salzer − *Department of Chemistry, Colorado State University, Fort Collins, Colorado 80523, United States;* orcid.org/0000-0003-0647-6205

Brian Diamond − *Department of Chemistry, Colorado State University, Fort Collins, Colorado 80523, United States;* Present Address: Department of Chemistry and Biochemistry, University of Oregon, Eugene, Oregon 97405, USA

Kelly Nieto − *Department of Chemistry, Colorado State University, Fort Collins, Colorado 80523, United States*

R. Colby Evans − *Department of Chemistry, Colorado State University, Fort Collins, Colorado 80523, United States*

Amy L. Prieto − *Department of Chemistry, Colorado State University, Fort Collins, Colorado 80523, United States;* orcid.org/0000-0001-9235-185X

Complete contact information is available at: https://pubs.acs.org/10.1021/acsaem.2c03573

Author Contributions

L.D.S. performed experiments, analyzed data, and wrote the manuscript. B.D. performed experiments and analyzed data. K.N. and A.L.P. assisted with coin cell measurements. R.C.E. assisted with materials synthesis and characterization. L.D.S., B.D., and J.B.S. designed experiments and wrote the manuscript. All authors have given approval to the final version of the manuscript.

Funding

This work was supported by the National Science Foundation (DMR-2046948).

Notes

The authors declare no competing financial interest.

■ ACKNOWLEDGMENTS

L.D.S. would like to thank Dakota Lorenz, Dan Windsor, and Brennan McBride for useful discussions and Prof. James Neilson for materials synthesis equipment. K.N. was supported in part through an American Dissertation Fellowship from the American Association of University Women (AAUW). A.L.P. and K.N. acknowledge support from the National Science Foundation (SSMC #1710672). We acknowledge CSU Analytical Core research facilities for data acquisition (SCR_021758).

■ REFERENCES

(1) Griffith, K. J.; Wiaderek, K. M.; Cibin, G.; Marbella, L. E.; Grey, C. P. Niobium Tungsten Oxides for High-Rate Lithium-Ion Energy Storage. *Nature* **2018**, *559*, 556−563.

(2) Burns, J. C.; Stevens, D. A.; Dahn, J. R. In-Situ Detection of Lithium Plating Using High Precision Coulometry. *J. Electrochem. Soc.* **2015**, *162*, A959.

(3) Downie, L. E.; Krause, L. J.; Burns, J. C.; Jensen, L. D.; Chevrier, V. L.; Dahn, J. R. In Situ Detection of Lithium Plating on Graphite Electrodes by Electrochemical Calorimetry. *J. Electrochem. Soc.* **2013**, *160*, A588.

(4) Vetter, J.; Novák, P.; Wagner, M. R.; Veit, C.; Möller, K.-C.; Besenhard, J. O.; Winter, M.; Wohlfahrt-Mehrens, M.; Vogler, C.; Hammouche, A. Ageing Mechanisms in Lithium-Ion Batteries. *J. Power Sources* **2005**, *147*, 269−281.

(5) Ribière, P.; Grugeon, S.; Morcrette, M.; Boyanov, S.; Laruelle, S.; Marlair, G. Investigation on the Fire-Induced Hazards of Li-Ion Battery Cells by Fire Calorimetry. *Energy Environ. Sci.* **2012**, *5*, 5271−5280.

(6) Deng, Q.; Fu, Y.; Zhu, C.; Yu, Y. Niobium-Based Oxides Toward Advanced Electrochemical Energy Storage: Recent Advances and Challenges. *Small* **2019**, No. 1804884.

(7) Ding, H.; Song, Z.; Zhang, H.; Zhang, H.; Li, X. Niobium-Based Oxide Anoes toward Fast and Safe Energy Storage: A Review. *Mater. Today Nano* **2020**, *11*, No. 100082.

(8) Griffith, K. J.; Harada, Y.; Egusa, S.; Ribas, R. M.; Monteiro, R. S.; Von Dreele, R. B.; Cheetham, A. K.; Cava, R. J.; Grey, C. P.; Goodenough, J. B. Titanium Niobium Oxide: From Discovery to Application in Fast-Charging Lithium-Ion Batteries. *Chem. Mater.* **2021**, *33*, 4−18.

(9) Roth, R. S.; Wadsley, A. D. Multiple Phase Formation in the Binary System Nb_2O_5−WO_3. I. Preparation and Identification of Phases. *Acta Crystallogr.* **1965**, *19*, 26−32.

(10) Roth, R. S.; Wadsley, A. D. Multiple Phase Formation in the Binary System Nb_2O_5−WO_3. II. The Structure of the Monoclinic Phases $WNb_{12}O_{33}$ and $W_5Nb_{16}O_{55}$. *Acta Crystallogr.* **1965**, *19*, 32−38.

(11) Andersson, S.; Wadsley, A. D. Crystallographic Shear and Diffusion Paths in Certain Higher Oxides of Niobium, Tungsten Molybdenum and Titanium. *Nature* **1966**, *211*, 581−583.

(12) Cava, R. J.; Murphy, D. W.; Zahurak, S. M. Lithium Insertion in Wadsley-Roth Phases Based on Niobium Oxide. *J. Electrochem. Soc.* **1983**, *130*, 2345.

(13) Koçer, C. P.; Griffith, K. J.; Grey, C. P.; Morris, A. J. Lithium Diffusion in Niobium Tungsten Oxide Shear Structures. *Chem. Mater.* **2020**, *32*, 3980−3989.

(14) Koçer, C. P.; Griffith, K. J.; Grey, C. P.; Morris, A. J. Cation Disorder and Lithium Insertion Mechanism of Wadsley−Roth Crystallographic Shear Phases from First Principles. *J. Am. Chem. Soc.* **2019**, *141*, 15121−15134.

(15) Griffith, K. J.; Grey, C. P. Superionic Lithium Intercalation through 2 Nm × 2 Nm Columns in the Crystallographic Shear Phase $Nb_{18}W_8O_{69}$. *Chem. Mater.* **2020**, *32*, 3860−3868.

(16) Saritha, D.; Pralong, V.; Varadaraju, U. V.; Raveau, B. Electrochemical Li Insertion Studies on $WNb_{12}O_{33}$—A Shear ReO3 Type Structure. *J. Solid State Chem.* **2010**, *183*, 988−993.

(17) Yan, L.; Lan, H.; Yu, H.; Qian, S.; Cheng, X.; Long, N.; Zhang, R.; Shui, M.; Shu, J. Electrospun WNb12O33 Nanowires: Superior Lithium Storage Capability and Their Working Mechanism. *J. Mater. Chem. A* **2017**, *5*, 8972−8980.

(18) Fuentes, A. F.; de la Cruz, A. M.; Torres-Martínez, L. M. A Study of Lithium Insertion in $W_4Nb_{26}O_{77}$: Synthesis and Characterization of New Phases. *Solid State Ionics* **1996**, *92*, 103−111.

(19) Fuentes, A. F.; Cruz, A. M. D. L.; Torres-Martinez, L. M. A Comparative Study of Lithium and Sodium Insertion in Two Block Structure Type Phases, W3Nb14O44 and W4Nb26O77. *MRS Online Proc. Libr. Arch.* **1996**, *453*, 659.

(20) Fuentes, A. F.; Garza, E. B.; de la Cruz, A. M.; Torres-Martínez, L. M. Lithium and Sodium Insertion in W3Nb14O44, a Block Structure Type Phase. *Solid State Ionics* **1997**, *93*, 245−253.

(21) Yang, Y.; Zhu, H.; Xiao, J.; Geng, H.; Zhang, Y.; Zhao, J.; Li, G.; Wang, X.-L.; Li, C. C.; Liu, Q. Achieving Ultrahigh-Rate and High-Safety Li+ Storage Based on Interconnected Tunnel Structure in Micro-Size Niobium Tungsten Oxides. *Adv. Mater.* **2020**, *32*, No. 1905295.
(22) Griffith, K. J.; Forse, A. C.; Griffin, J. M.; Grey, C. P. High-Rate Intercalation without Nanostructuring in Metastable Nb_2O_5 Bronze Phases. *J. Am. Chem. Soc.* **2016**, *138*, 8888−8899.
(23) Cheetham, A. K.; Allen, N. C. Cation Distribution in the Complex Oxide, $W_3Nb_{14}O_{44}$; a Time-of-Flight Neutron Diffraction Study. *J. Chem. Soc., Chem. Commun.* **1983**, *3*, 1370−1372.
(24) Jiang, J.; Li, Y.; Liu, J.; Huang, X.; Yuan, C.; Lou, X. W. Recent Advances in Metal Oxide-Based Electrode Architecture Design for Electrochemical Energy Storage. *Adv. Mater.* **2012**, *24*, 5166−5180.
(25) Itou, Y.; Ogihara, N.; Kawauchi, S. Role of Conductive Carbon in Porous Li-Ion Battery Electrodes Revealed by Electrochemical Impedance Spectroscopy Using a Symmetric Cell. *J. Phys. Chem. C* **2020**, *124*, 5559−5564.
(26) Aurbach, D.; Levi, M. D.; Levi, E. A Review on the Solid-State Ionics of Electrochemical Intercalation Processes: How to Interpret Properly Their Electrochemical Response. *Solid State Ionics* **2008**, *179*, 742−751.
(27) Wen, C. J.; Boukamp, B. A.; Huggins, R. A.; Weppner, W. Thermodynamic and Mass Transport Properties of "LiAl". *J. Electrochem. Soc.* **1979**, *126*, 2258−2266.

https://doi.org/10.1021/acsaem.2c03573
ACS Appl. Energy Mater. XXXX, XXX, XXX−XXX